

Supporting information

Direct band gap germanium microdisks obtained with silicon nitride stressor layers

Moustafa El Kurdi,¹ Mathias Prost,¹ Abdelhamid Ghrib,¹ Sébastien Sauvage,¹ Xavier Checoury,¹ Grégoire Beaudoin,² Isabelle Sagnes,² Gennaro Picardi,³ Razvigor Ossikovski,³ and Philippe Boucaud¹

1) Institut d'Electronique Fondamentale, CNRS, Univ. Paris-Sud, Université Paris-Saclay, Bâtiment 220, Rue André Ampère, F-91405 Orsay, France

2) Laboratoire de Photonique et de Nanostructures, CNRS - UPR20, Route de Nozay, F-91460 Marcoussis, France

3) Laboratoire de Physique des Interfaces et des Couches Minces, CNRS, Ecole polytechnique, Université Paris-Saclay, F-91128 Palaiseau, France

Supplementary 1: Modeling of microdisk strain field by finite element

The strain field in the microdisks was modeled by finite elements using the COMSOL software packages following the method presented in Ref. [1]. Figure S1 (a) shows a cross-section of the in-plane components $(\varepsilon_r + \varepsilon_\theta)/2$ obtained for the 6 μm diameter microdisk while Fig. S1 (b) shows the variation of the strain along one radius 10 nm below the top Ge surface.

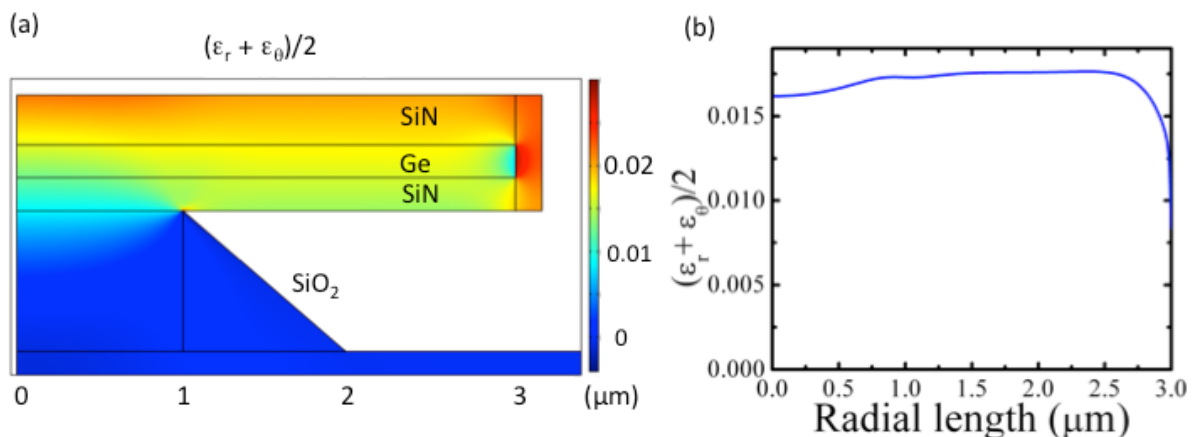


Figure S1: (a) Cross-section of the biaxial strain field $(\epsilon_r + \epsilon_\theta)/2$ calculated by finite elements. (b) Strain field along one disk radius recorded 10 nm below the surface. The 0 position corresponds to the disk center.

The calculated strain is larger than in Ref. 1 (1.75% biaxial strain instead of 1.3% biaxial strain). This is a direct consequence of the smaller thickness of the Ge film, 190 nm in these structures instead of 500 nm in Ref. [1], leading to a better stress transfer. As in Ref. [1], the calculated strain is slightly below the one obtained by Raman spectroscopy. The finite element modeling also indicates that the strain field is larger in the 6 μm microdisk as compared to the 9 μm microdisk because of a smaller pedestal.

Supplementary 2: Modeling of disk temperature

The microdisk temperature was modeled by using a Finite Element Modeling of heat transfer with a fixed cooling temperature of the substrate in a 2D axisymmetric geometry. The optical pumping of the μ -disk is modeled as a heating source distributed onto a 3 μm diameter disk, corresponding to the estimated waist of the laser beam on the disk surface and in a depth of 50 nm corresponding to the optical absorbing length of the germanium layer. Assuming a 2.6 mW of incident optical power and considering a surface reflectivity of 45% one deduces a heating power density of $Q_{pump} = 4 \times 10^{-3} \text{ W}/\mu\text{m}^3$. The temperature of the microdisk results from a balance between the temperature cooling from the substrate and the heating source which results from the optical pumping. We note that a high temperature gradient occurs in the disk pedestal because it corresponds to the main heat transfer path between the disk and the substrate. The heat transfer between the disk and the substrate is then mainly dependent on the silicon oxide pedestal size and thermal conductivity. The thermal conductivity of the silicon oxide is not constant with temperature. It varies from 1.38 W/(m K) at room temperature down to 0.1 W/(m K) at 10K. This leads to a nonlinear behavior of the disk temperature versus the cooling temperature of the substrate. The thermal conductivity dependence with temperature $k(T)$ for the silicon oxide is thus introduced in the modeling, following experimental and theoretical results as reported in Ref. [2]. One can interpolate the findings of Ref. [2] with a polynomial law.

For the Ge layer and the silicon nitride, we used a thermal conductivity of 58 W/(m K) and 20 W/(m K) respectively. In Figure S2a we show the temperature distribution assuming a substrate temperature of 10 K and $Q_{pump} = 4 \times 10^{-3} \text{ W}/\mu\text{m}^3$. As discussed above, the temperature in the substrate and in the disk are nearly constant but highly inhomogeneous in the disk pedestal where the heat flux takes place. We report on Fig. S2b the microdisk temperature with respect to the cooling temperature of the substrate. The dashed line is a guide to show the deviation of the disk temperature from the substrate temperature. The inset shows the temperature difference ΔT between both. As can be seen, the disk heating depends non-linearly on the substrate temperature as a consequence of the silicon oxide dependence of the thermal conductivity. The minimum temperature that can be reached in

the disk is around 120 K when the substrate is cooled down to 10 K while at room temperature the disk temperature is increased by 37 K up to 330 K.

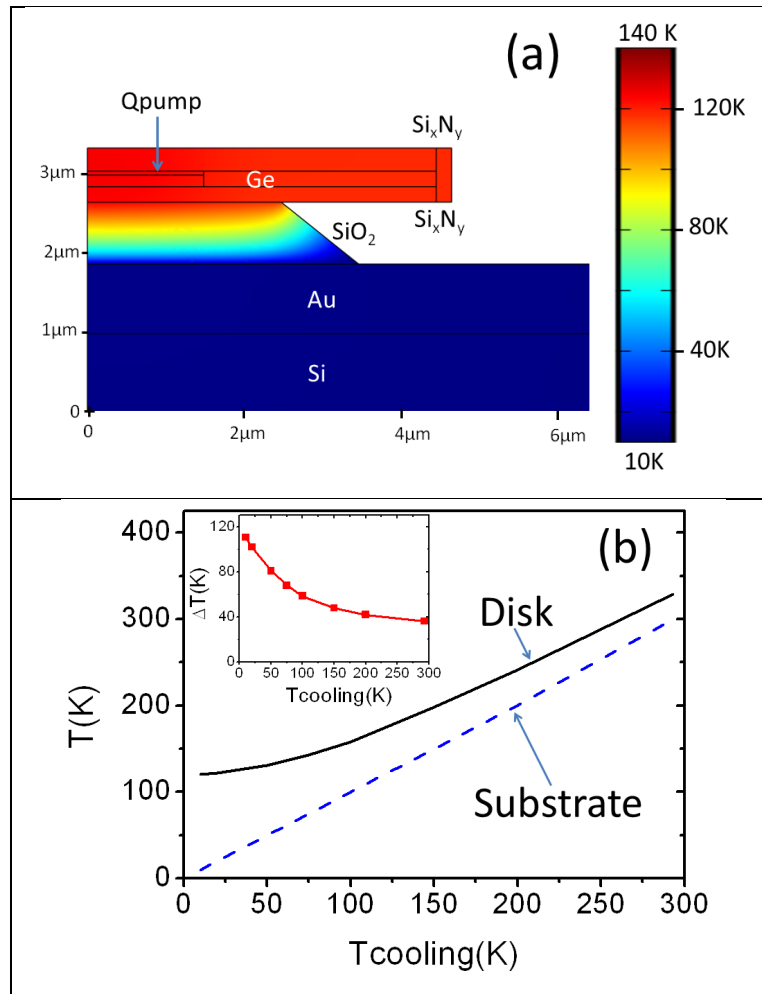


Figure S2 (a) Distribution of temperature of the bonded disk under an optical pumping and with a cooled temperature of the substrate of 10K (b) Temperature of the disk under optical pumping with respect to the cooling temperature of the substrate from 10K to 300K, the inset shows the difference between the disk temperature and the cooling temperature.

Supplementary 3: Carrier density dependence with temperature

The modeling of the PL signal of the strained microdisk with temperature accounts for the carrier recombination dynamics, i.e. it includes the excess carrier density dependence with temperature.

To examine the carrier density variation with temperature, we first investigate the case of an unstrained germanium layer of the bonded sample without processing into disk, i.e. on a plain surface of the sample. In this case, the silicon nitride stressor does not relax its internal stress and the Ge layer remains nearly unstrained. The PL spectrum evolution with

temperature of the bonded Ge layer is shown in figure S3a. At room temperature, the spectrum is dominated by the direct transition at 1560 nm wavelength. This contribution quenches rapidly as the temperature is decreased. The indirect contribution occurs at 1790 nm at room temperature and dominates the spectrum at low temperature with an increasing amplitude factor of 30 at 12 K. The direct and indirect intensities as obtained from the PL spectra are reported in Fig. S3b in values normalized by the room temperature case. The indirect transition, which stems from non-vertical transitions in the k-space can be modeled following a convolution integral of the respective density of states $\rho_C(E)$ and $\rho_V(E)$ of the conduction and the valence bands weighted by the carrier distribution function $f_C(E)$ for electrons and $f_V(E)$ for holes following this expression [3]

$$I_{ind}(h\nu) \propto \int_0^\infty f_C(E)\rho_C(E)f_V(h\nu - E_G - E)\rho_V(h\nu - E_G - E)dE \quad \text{Eq. S3a}$$

In this expression E_G is the effective energy of the indirect band gap including the electronic band gap energy and the assisting phonon energy, *i.e.* $E_G = (E_L - E_V) \pm E_{phonon}$ with E_L the L conduction band energy and E_V the valence band energy.

We have performed a calculation of the indirect transition intensity following Eq. S3a with an adjustment of the injected carrier densities such that the evolution with temperature fits the experimental result (full blue line in figure S3b). The normalized lifetime and thus carrier density dependence with temperature used to fit the experimental result by using Eq. S3a is reported in Fig. S3c. We use the same carrier density evolution to calculate the direct transition dependence with temperature and considering a splitting energy of 136 meV in the conduction band to calculate the electron population in the gamma valley. The result of the calculation is reported on Fig. S3b (black full line). As can be seen, the calculation is in satisfying agreement with the experimental measurement for the direct transition thus giving consistency to the carrier density variation as reported in Fig. S3c.

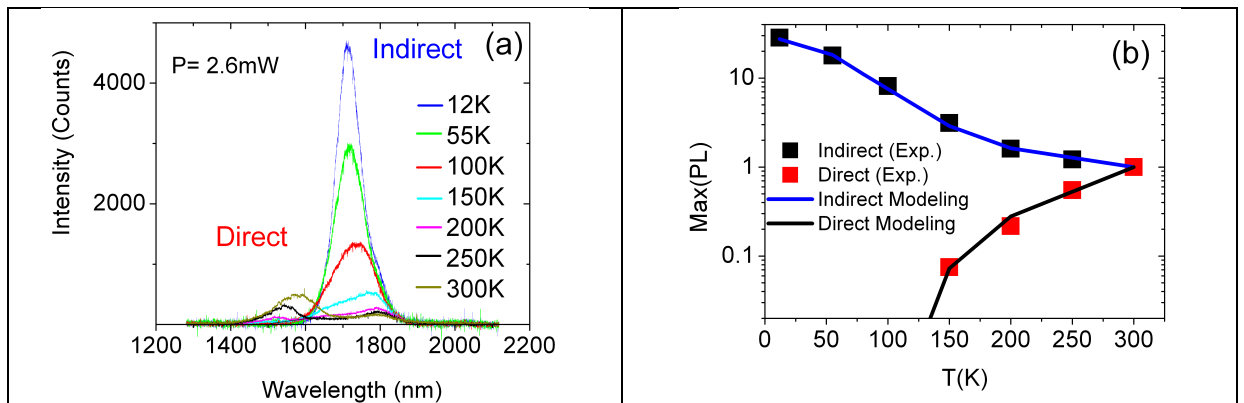


Figure S3 (a) Photoluminescence spectra obtained from the bonded Ge layer but without processing into microdisk (plain surface) (b) The contributions from direct transition and indirect transitions are reported by red and black squares respectively, the values are normalized to the intensity of uncooled sample (room temperature). The full blue line is the dependence with temperature of

indirect recombination as obtained with eq. S3 by adjusting the carrier densities. The black full line is the temperature dependence of the direct transition calculated with the carrier densities as obtained from the analysis of the indirect transition.

The variation of out-of-equilibrium injected carrier density vs. temperature can be well modeled in the framework of a Shockley-Read-Hall (SRH) formalism. We assume that the generated carrier densities n_{ex} at fixed pumping power are directly linked to the non-radiative lifetime following the generation-recombination balance such that $n_{ex} = G \times \tau$ where τ is the non-radiative lifetime and G the generation rate.

We account for both Auger process for doped sample and for carrier capture by trap level in a SRH modeling such as

$$\tau = \frac{1}{(\tau_{Auger})^{-1} + (\tau_{SRH})^{-1}} \quad \text{Eq. S3b}$$

With

$$\frac{1}{\tau_{Auger}} = C_n N_d^2 \quad \text{Eq. S3c}$$

The Shockley-Read-Hall recombination time, for a n-doped sample with a Fermi level F0 can be expressed as [4]

$$\tau_{SRH} = \tau_{p0} \left(1 + e^{(ET-F0)/k_B T} \right) \quad \text{Eq. S3d}$$

With ET the trap level energy, $F0$ the Fermi energy level at equilibrium and τ_{p0} a minority carrier capture lifetime. Thus the carrier density dependence with temperature can be well reproduced by calculating the evolution of the non-radiative lifetime τ following Eq. S3b and d. The result of the calculation normalized to the lifetime calculated at room temperature $\tau(300K) = 2ns$ is reported in figure S3c. We obtain a very good agreement with the experiments with $\tau_{Auger} = 14 ns$ which corresponds to an Auger coefficient $C_n = 0.9 \times 10^{-30} cm^6 s^{-1}$, a trap level energy such that $ET-F0 = 0.023 eV$ and with a reasonable value for minority capture time $\tau_{p0} = 750 ps$. [5] The trap level is found close to $F0$ and consequently close to the conduction band edge, due to n-type doping. This suggests that the SRH lifetime should be controlled by a carrier capture process involving shallow traps. We highlight the consistency between the carrier lifetime found by applying the present analysis $\tau(300K) = 2 ns$ and by measurements using time-resolved spectroscopy performed on Ge layers [6]. In the latter reference, the typical reported values were also in the few ns range for different types of Ge samples.

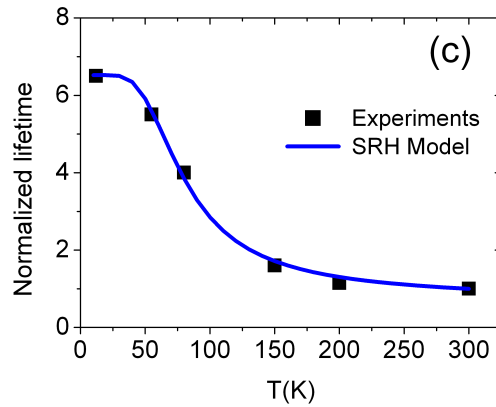


Figure S3 (c) Normalized lifetime corresponding to the carrier density evolution as a function of temperature. Squares are obtained from the analysis of the indirect transition on unstrained Ge layers and the full line results from SRH modeling. The values are normalized with the one at room temperature.

References

- [1] Ghrib, A.; El Kurdi, M.; Prost, M.; Sauvage, S.; Checoury, X.; Beaudoin, G.; Chaigneau, M.; Ossikovski, R.; Sagnes, I.; Boucaud, P. All-Around SiN Stressor for High and Homogeneous Tensile Strain in Germanium Microdisk Cavities. *Adv. Opt. Mater.* **2015**, *3*, 353–358.
- [2] Asheghi, M.; Touzelbaev, M. N.; Goodson, K. E.; Leung, Y. K.; Wong, S. S. Temperature-Dependent Thermal Conductivity of Single-Crystal Silicon Layers in SOI Substrates. *Trans. ASME* **120**, 30 (1998).
- [3] Wagner, J.; Viña, L. Radiative recombination in heavily doped p-type germanium. *Phys. Rev. B* **1984**, *30*, 7030.
- [4] Shockley, W.; Read, W.T. Statistics of the Recombinations of Holes and Electrons. *Phys. Rev. B* **1952**, *87*, 835.
- [5] Hellings, G.; Eneman, G.; Krom, R.; De Jaeger, B.; Mitard, J.; De Keersgieter, A.; Hoffmann, T.; Meuris, M.; de Meyer, K. Electrical TCAD Simulations of a Germanium pMOSFET Technology. *IEEE Trans. Electron Devices* **2010**, *57*, 2539-2546.
- [6] Geiger, R.; Frigerio, J.; Suess, M. J.; Chrastina, D.; Isella, G.; Spolenak, R.; Faist, J.; Sigg, H. Excess carrier lifetimes in Ge layers on Si. *Appl. Phys. Lett.* **2014**, *104*, 062106.